Atomic-Scale Engineering | Hot Paper

Deutsche Ausgabe: DOI: 10.1002/ange.201511360
Internationale Ausgabe: DOI: 10.1002/anie.201511360

Low-Temperature Cationic Rearrangement in a Bulk Metal Oxide

*Man-Rong Li, Maria Retuerto, Peter W. Stephens, Mark Croft, Denis Sheptyakov, Vladimir Pomjakushin, Zheng Deng, Hirofumi Akamatsu, Venkatraman Gopalan, Javier Sánchez-Benítez, Felix O. Saouma, Joon I. Jang, David Walker, and Martha Greenblatt**

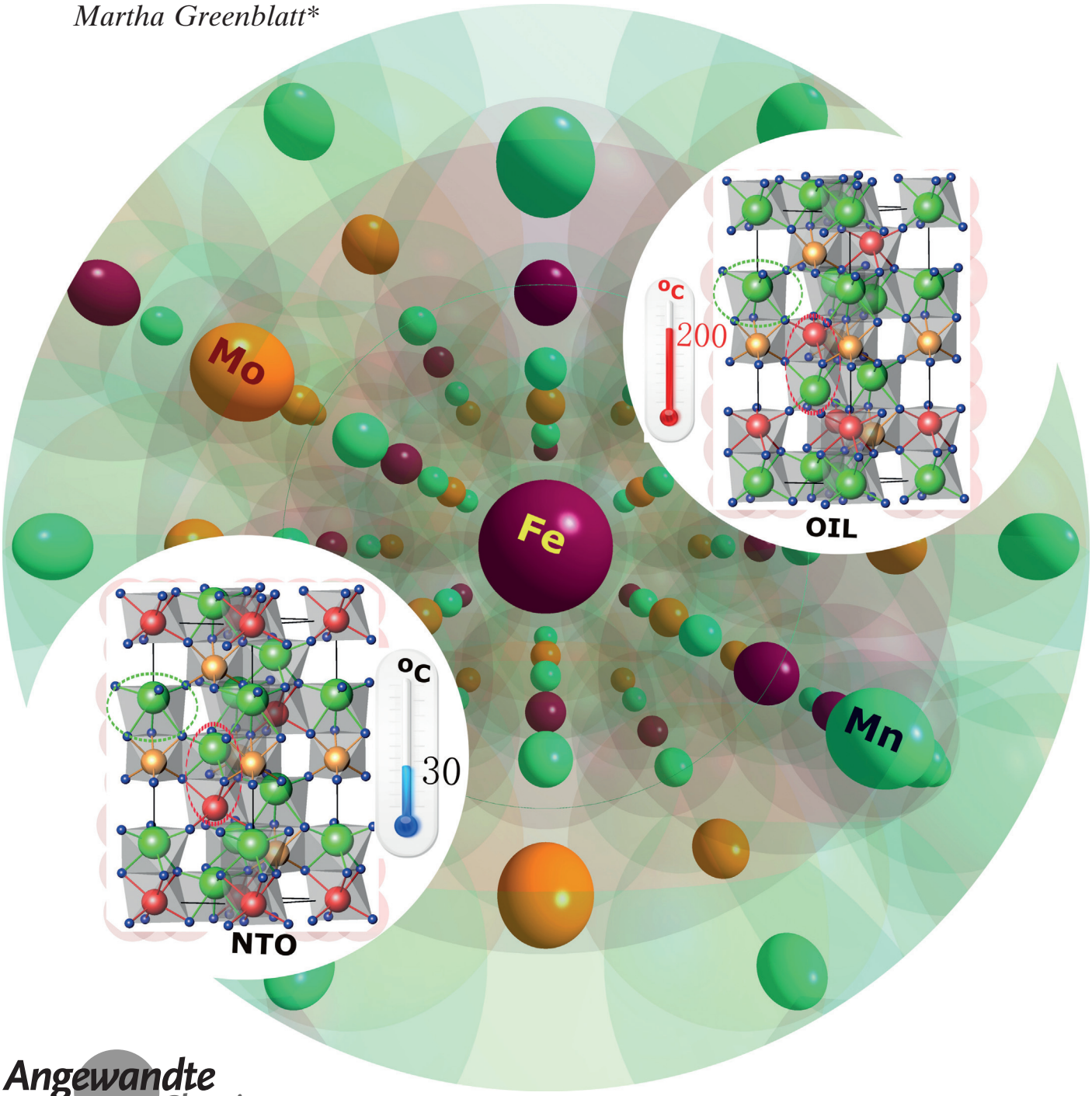

Abstract: *Cationic rearrangement is a compelling strategy for producing desirable physical properties by atomic-scale manipulation. However, activating ionic diffusion typically requires high temperature, and in some cases also high pressure in bulk oxide materials. Herein, we present the cationic rearrangement in bulk Mn_2FeMoO_6 at unparalleled low temperatures of 150–300 °C. The irreversible ionic motion at ambient pressure, as evidenced by real-time powder synchrotron X-ray and neutron diffraction, and second harmonic generation, leads to a transition from a Ni_3TeO_6–type to an ordered-ilmenite structure, and dramatic changes of the electrical and magnetic properties. This work demonstrates a remarkable cationic rearrangement, with corresponding large changes in the physical properties in a bulk oxide at unprecedented low temperatures.*

The physical properties of transition metal oxides can be controlled by atomic-scale engineering.[1–4] One common strategy to control the cationic distribution and environment for desired applications in bulk oxides is to manipulate the displacive transitions (polyhedral distortions and cooperative tilting/rotation), or the cationic rearrangements.[5,6] Displacive transitions can arise at relatively low temperatures,[7] while cationic rearrangements generally require high temperatures to overcome large energy barriers.[5,8–11] Cationic rearrangements below 300 °C have only been reported in nanocrystals,[12–14] or when driven by applied external electrical potential as in battery materials,[15,16] but not in bulk metal oxides by temperature alone. The corundum-derived $A_2BB'O_6$ family of compounds can incorporate transition metal ions at all of the cationic sites and adopt different cation order–disorder configurations, providing an ideal platform for materials engineering.[5,8,9,17–22] Recently, the polar room-temperature ($T_C \approx 337$ K) ferrimagnet Mn_2FeMoO_6, hereafter called phase I, was prepared by quenching to room temperature from 1350 °C at a pressure of 8 GPa.[21] First-principles calculations indicated that the band gap, the magnetic and electronic properties, and the ground-state energy of Mn_2FeMoO_6 are governed by the arrangement of cations in the unit cell, which suggested effective property control through cationic arrangement. In this work, we have found dramatic cationic movement when phase I was heated under ambient pressure. Although this cationic rearrangement does not significantly change the overall metal–oxygen connections, nevertheless, it produces strong modifications of the magnetic and electronic properties.

Initial thermal analyses on phase I of Mn_2FeMoO_6 indicated no decomposition up to 575 °C at ambient pressure, but showed unexpected lattice parameter and diffraction peak evolution when annealed above 175 °C (Supporting Information, Figure S1). Figures 1 a and S2 show selected in situ variable-temperature synchrotron powder X-ray diffraction (SPXD) patterns that highlight the structural changes. This peak evolution was irreversible, as reflected by the patterns after the sample was cooled down from 327 °C to room temperature (hereafter the Mn_2FeMoO_6 annealed in ambient pressure at 327 °C is called phase II). It is noteworthy that, similar to that of phase I, all of the in situ variable-temperature SPXD patterns can be indexed with a general corundum-related $R3$ or $R\bar{3}$ symmetry. The unusual temperature-dependent peak evolution is due to the large variation of lattice parameters illustrated in Figure 1 b. Both a and c expand gradually up to ≈190 °C and also above ≈275 °C, but deviate from linearity over the intermediate temperature region, rendering small contraction in the ab-plane and a much larger expansion along the c-axis (Figure 1 b). Both room-temperature and in situ variable-temperature second harmonic generation (SHG) from phase II (Figure S3a) and phase I (Figure S3b) eliminate the centrosymmetric ilmenite structure. Rietveld refinements on selected SPXD data (Table S1) could not draw a firm conclusion of the structural type. However, combined Rietveld refinements of the room-temperature SPXD and powder neutron diffraction (PND) data of phase II yielded a good fit in the ordered-ilmenite model (Figure 2 a and Tables S2–3), but not for the Ni_3TeO_6 structure type (Figure S4). Compared with the Ni_3TeO_6-structure of phase I,[21] in the ordered ilmenite-type of phase II the atomic occupancy within the face-sharing $Mn1O_6/MoO_6$ octahedral pairs are statistically unchanged, while 88(1)% of Mn2 and Fe within the face-sharing

[*] Dr. M. R. Li, M. Retuerto, Z. Deng, Prof. M. Greenblatt
Department of Chemistry and Chemical Biology
Rutgers, the State University of New Jersey
610 Taylor Road, Piscataway, NJ 08854 (USA)
E-mail: martha@rutchem.rutgers.edu
Prof. P. W. Stephens
Department of Physics & Astronomy
State University of New York
Stony Brook, NY 11794 (USA)
Prof. M. Croft
Department of Physics & Astronomy
Rutgers, the State University of New Jersey
136 Frelinghuysen Road, Piscataway, NJ 08854 (USA)
Dr. D. Sheptyakov, V. Pomjakushin
Laboratory for Neutron Scattering and Imaging
Paul Scherrer Institut
5232 Villigen PSI (Switzerland)
Dr. H. Akamatsu, V. Gopalan
Department of Materials Science and Engineering
Pennsylvania State University
University Park, PA 16802 (USA)
Dr. J. Sánchez-Benítez
Departmentto de Química Física I
Facultad de Ciencias Químicas
Universidad Complutense de Madrid
28040 Madrid (Spain)
F. O. Saouma, Prof. J. I. Jang
Department of Physics, Applied Physics and Astronomy
Binghamton University
P.O. Box 6000, Binghamton, NY 13902 (USA)
Prof. D. Walker
Lamont-Doherty Earth Observatory
Columbia University
61 Route 9W, Palisades, NY 10964 (USA)

Supporting information for this article can be found under:
http://dx.doi.org/10.1002/anie.201511360.

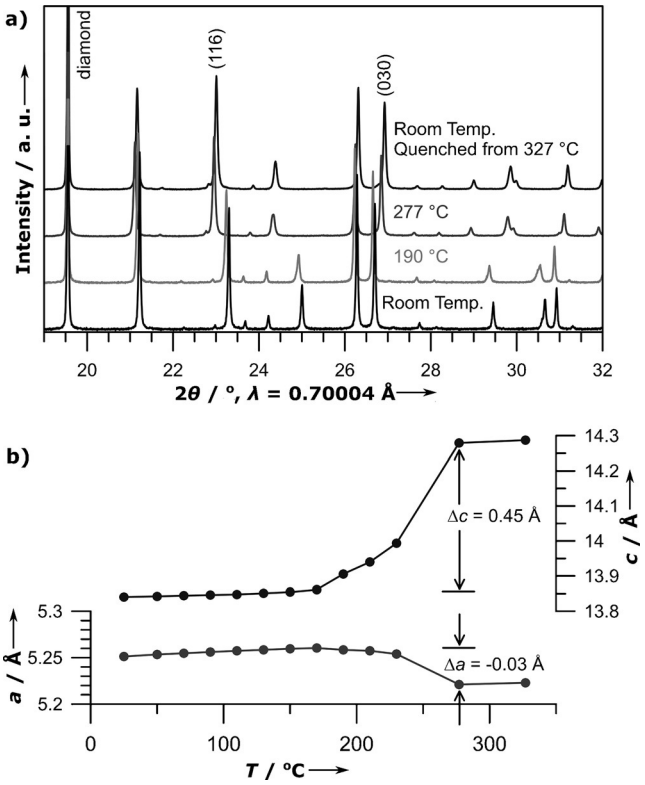

Figure 1. a) Selected in situ variable-temperature SPXD patterns at room temperature, 190 °C, and 277 °C, and at room temperature after cooling from 327 °C (phase II) to show the irreversible peak evolution. The (116) reflection at ≈22.9° moves to lower angle, while the (030) reflection at ≈26.8° to higher angle. b) Evolution of the lattice parameters extracted from the in situ variable-temperature SPXD up to 327 °C, showing contraction in the *ab*-plane (*a* contraction (Δa) around −0.03 Å) and large expansion along *c* (*c* expansion (Δc) around 0.45 Å) between 175 and 275 °C, giving ≈1.3 % larger cell volume.

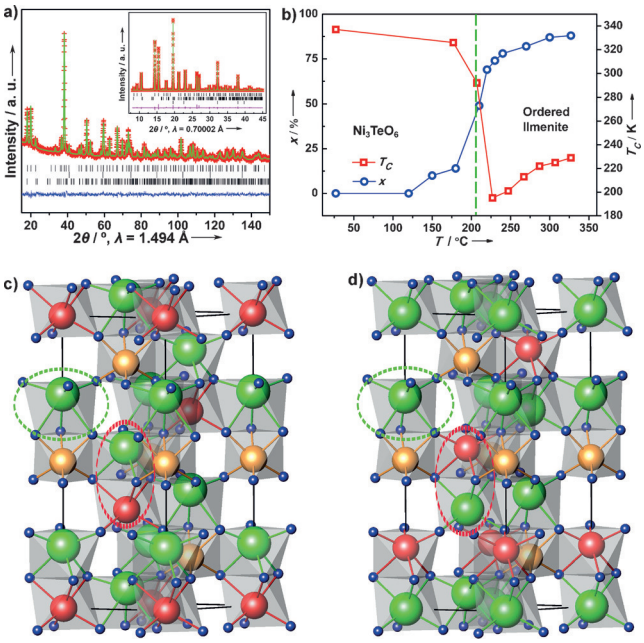

Figure 2. a) Plots of the room-temperature PND data of phase II from combined PND and SPXD refinements. The vertical bars (|) indicate the index of phase II, vanadium, and small wolframite-type impurity $MnMoO_4$, respectively, from top to bottom. Inset shows plots of the room-temperature SPXD data from combined refinements. The vertical bars (|) indicate phase II, small wolframite impurity, and diamond, respectively, from top to bottom. b) Variation of the Fe and Mn (at the Mn2-site) occupancy (*x*) in $[(Mn1)(Mn2_{1-x}Fe_x)][(Mn2_xFe_{1-x})(Mo)]O_6$ upon heating, and the corresponding magnetic T_C evolution for samples annealed at different temperatures up to 327 °C. Note that the *x* value at 327 °C is from the combined refinements shown in Figure 2a. The dashed line marks the boundary between Ni_3TeO_6 (phase I) and ordered ilmenite (phase II) structures. c) Ni_3TeO_6 type crystal structure at 150 °C ($x = 0.10(1)$). d) Ordered-ilmenite-type crystal structure at 300 °C ($x = 0.88(1)$). Green spheres represent Mn, red are Fe, orange are Mo, and blue are oxygen (plotted smaller for clarity). The green dashed-line ellipse highlights the distortion degree of Mn1O6 for comparison; the red dashed-line ellipse encloses the face-sharing Mn2O6/FeO6 octahedral pairs along the *c*-axis.

$Mn2O_6/FeO_6$ pairs switched positions (Table S2), giving a nominal structural formula of $[(Mn1)(Mn2_{0.12(1)}(Fe_{0.88(1)})][(Mn2_{0.88(1)}Fe_{0.12(1)})(Mo)]O_6$. There was no cation mixing over the Mo-site detected within the statistical uncertainty. Structural analysis of the low-temperature PND data showed a structure of phase II down to 1.72(5) K (Figure S5 and Tables S2–3). Compared with phase I (Table S3), the cationic switching yields shortened (≈0.10(1) Å) average metal–oxygen distance at the original Mn2-site (now dominated by 88(1)% Fe^{3+}), but lengthened (≈0.08(1) Å) value of the Fe-site (now dominated by 88(1)% Mn^{2+}), owing to the ionic radius differences between the high-spin Mn^{2+} (0.83 Å) and Fe^{3+} (0.645 Å) at octahedral sites.[23] This finding is consistent with the absence of charge transfer in $Mn^{2+}{}_2Fe^{3+}Mo^{5+}O_6$, as seen by comparison of the X-ray absorption near-edge spectra (XANES) of phase I and phase II (Figure S6).

The above studies on a Mn_2FeMoO_6 phase II sample indicated irreversible cationic rearrangement upon heating, accompanied by structural transition from the Ni_3TeO_6-type to the ordered ilmenite-type structure. To further investigate the cationic rearrangement, in situ variable-temperature PND was undertaken by heating phase I. These measurements (Figures S7–8) are in good agreement with the in situ variable temperature SPXD results (Figure 1 a,b). Writing the chemical formula as $[(Mn1)(Mn2_{1-x}Fe_x)][(Mn2_xFe_{1-x})(Mo)]O_6$, $x = 0$ corresponds to the Ni_3TeO_6 structure (with layers of Mn:Fe alternating with layers of Mn:Mo along the *c* axis), while $x = 1$ would be a fully ordered ilmenite phase, with segregated layers of Mn and Fe:Mo. *x* is plotted as a function of temperature in Figure 2b: below 127 °C, there is no ionic motion ($x = 0$) within the accuracy of the measurements. Although the unusual lattice parameter evolution (deviation from linearity in Figures 1b and S7) appears around 190 °C, 10 % of Mn2 and Fe have switched their positions already at 150 °C, based on the PND data. The value of *x* increases to approximately 50 % at 210 °C, and 87 % at the highest temperature measured, 300 °C, in good agreement with its value for the phase II. As the Fe^{3+} and $Mn2^{2+}$ ions change places, the metal–oxygen distances also evolve, so that the Fe^{3+}–O distances are always smaller than the $Mn2^{2+}$–O distances. The change in the Mn1–O and Mo–O distances

over that temperature range are a factor of five times smaller. This cationic rearrangement finally gives a smaller structural distortion in phase II, which results in a smaller estimated spontaneous polarization along the c axis (55 $\mu C\,cm^{-2}$)[24] compared with that of phase I (68 $\mu C\,cm^{-2}$).[21] This variation of structure distortion can be seen from the crystal structures at 150 (Figure 2c) and 300 °C (Figure 2d) by comparing the octahedra enclosed in the dashed green lines.

The cationic rearrangement in Mn_2FeMoO_6 produces dramatic changes in the physical properties. Figure 3a illustrates the magnetization (M) versus temperature (T) evolution at $H = 0.1$ T for Mn_2FeMoO_6 prepared at high pressure (phase I), and the phases annealed at 207, 227, 267, and 327 °C (phase II). The evolution of the magnetic transition temperature (also plotted in Figures 2b and S9 and listed in Table S6) coincides with the Mn/Fe switching degree (x). The T_C decreases in phase I as the degree of disorder increases between cations, as reported in Sr_2FeMoO_6 perovskite,[25] and strongly drops when the structural transition occurs. Then it starts increasing again as the degree of cationic order increases in the phase II region. The hysteresis loops (Figure 3b) show ferromagnetic response in both phase I and II at 5 K, but paramagnetic behavior for the latter at 300 K. The magnetic structures of phases I and II, as determined by PND, are shown in Figure 3c and d, respectively. All of the spins in both phases are oriented along c. In phase II, the direction of the magnetic moments of Mn2 and Fe ions have switched relative to those of phase I. The magnetic structure of phase II is formed by alternating ferromagnetic layers of Mn1 (2.8(3) μ_B) and Mn2 (2.6(4) μ_B) with those of Fe (−1.6(1) μ_B) and Mo (−0.82(6) μ_B); these ferromagnetic layers are arranged antiferromagnetically along the c-axis. The magnitude of the net magnetic moment ($\approx$2.98(4) μ_B/f.u.) of phase II obtained by PND is comparable to that obtained by the magnetic measurements ($\approx$3.5 μ_B/f.u.).

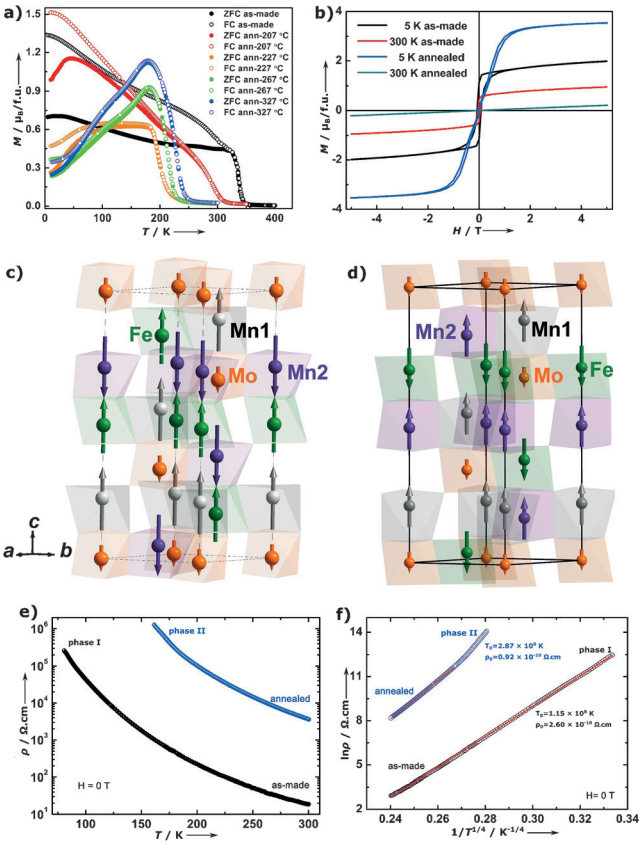

Figure 3. a) M vs. T in the ZFC and FC modes under $H = 0.1$ T for the phase directly prepared at high pressure (phase I), and the phase annealed at 207, 227, 267, and 327 °C (phase II) to show the magnetization and T_C evolution: T_C decreases in the Ni_3TeO_6 structural region from 337 K (phase I) to 195 K when annealed up to 227 °C, and then starts to increase from 201 to 229 K (phase II) when annealed between 247 °C and 327 °C. b) M vs. H curves recorded at $T = 5$ and 300 K for phases I and II. The value of the net magnetic moment at 5 T in phase II is substantially larger ($\approx$3.5 μ_B/f.u.) than in phase I ($\approx$2 μ_B/f.u.). c) Magnetic structure of phase I at 10 K refined from PND data. Net magnetic moment: M = m(Mn1) + m(Fe) − m(Mn2) − m(Mo). d) Magnetic structure of phase II at 1.72 K refined from PND data. Net magnetic moment: M = m(Mn1) + m(Mn2) − m(Fe) − m(Mo). e) ρ vs. T at zero-field shows semiconductor behavior of phase I and II. f) The linear fit to the plots of lnρ vs. $1/T^{1/4}$, indicating Mott's variable range hopping conduction mechanism in both phase I and II. Note that the magnetic structure, and magnetic and magnetotransport data of phase I are from Ref. [21].

In Figure 3e, the resistivity (ρ) versus temperature (T) plots indicate 20 Ω cm and 3.6×10^3 Ω cm at 300 K for phases I and II, respectively at $H = 0$ T. The resistivity becomes too high to be measured below 160 K in phase II. Above 200 K, the resistivity of phase II also follows a Mott's variable range hopping[26] conduction mechanism, as seen in the linear fit of lnρ versus $1/T^{1/4}$ plot (red line in Figure 3f, $T_0 = 2.87 \times 10^8$ K, $\rho_0 = 0.92 \times 10^{-10}$ Ω cm), the same behavior as phase I. Below 200 K, the limited data range does not allow any reasonable fit. Thus, phase II is also a ferrimagnetic variable range hopping semiconductor, but with around three orders of magnitude larger resistivity than phase I. The optical band-gap of phase II can be roughly estimated from the SHG counts, where it steeply increases in Figure S3a, to between 800–900 nm (1.38–1.55 eV).[27]

The corundum-derived crystal structures under high pressure can crystallize in the structural type of the smallest possible cell volume by the arrangement of edge-sharing octahedra between the larger and smaller cations in the ab-plane, at a cost of lattice strain owing to ion size mismatch.[5,28–30] Compared with the cationic re-distribution in spinel nanocrystals at moderate temperature (typically 350–600 °C),[12–14] electric potential-driven ionic motion in battery materials,[15,16] and ionic rearrangements in bulk oxides (typically above 600 °C),[10,11] the lattice-strain-driven cationic rearrangement in Mn_2FeMoO_6 at such low temperatures (150–300 °C) is unique. In the Ni_3TeO_6-type phase I, the smaller cell volume is achieved by edge-sharing between the larger Mn^{2+} (0.83 Å) and smaller Fe^{3+} (0.645 Å) or Mo^{5+} (0.61 Å)[23] in the ab-plane. The position swap between Mn2 and Fe within the face-sharing octahedral pairs result in the elongation of the c-axis, and alternating layers of the larger $Mn1^{2+}O_6$–$Mn2^{2+}O_6$ edge-sharing octahedra with the smaller $Fe^{3+}O_6$–$Mo^{5+}O_6$ octahedra in the ab-plane. This structural change relieves the lattice strain, as reflected by the degree of octahedral distortion (Figure 2c,d and Table S5), and lowers the energy of the material. The change in the crystal structure

also produces a change in the magnetic arrangement by switching the direction of Mn2 and Fe spins, but keeping the same global ferrimagnetic structure.

To understand this structural rearrangement, it is necessary to find a mechanism; it is simply not plausible that the Mn^{2+} and Fe^{2+} ions exchange in a single step through their shared face. Figure 4 illustrates one possible pathway from

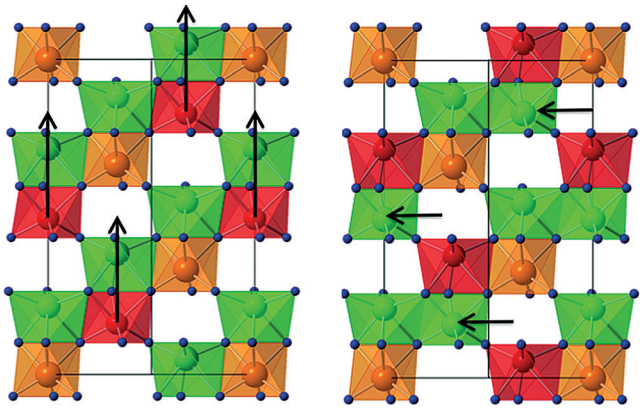

Figure 4. Possible mechanism for the transformation from Ni_3TeO_6 to ordered ilmenite structure type. Views of the Ni_3TeO_6 (left) and ordered ilmenite (right) structure types along [1-10]. Black arrows illustrate the motion of metal ions. Colors: Mn green, Fe red, Mo orange, and O blue.

the Ni_3TeO_6 to the ordered-ilmenite structure. Starting with the Ni_3TeO_6 structure on the left, in the first step, Mn^{2+} and Fe^{3+} ions move one layer in the *c* direction. Subsequently, Mn^{2+} ions move to adjacent empty sites in the same layer to produce the ordered-ilmenite structure type at the right. There are several equivalent sets of motions that achieve the same result, and it is likely that the failure of the material to achieve a fully ordered ilmenite structure at the temperatures studied is related to the one-way transition path nucleated at multiple sites in each grain.

Our results established an unprecedented lattice-strain-driven large cationic motion and atomic-scale physical property tuning in a bulk oxide at exceptionally low temperature ranges (150–300 °C). A possible cationic switching reversibility under high pressure is worthy of further exploration at in situ elevated temperature and pressure, to understand the ionic motion cycle and the structure evolution in the corundum family in the Earth's mantle. Deep in the Earth, conditions favor highly ordered $LiNbO_3$-type structures, which are, however, very rare in the shallow crust compared with the ilmenite-related minerals.

Experimental Section

See the Supporting Information for Experimental Details: Materials and Methods; thermal stability; in situ variable-temperature SPXD, PND, and SHG; XANES; crystallographic data and analyses; and temperature-dependent magnetic transition temperature evolution.

Acknowledgements

This work was supported by the NSF-DMR-1507252 grant. J. S.-B. is supported by the Spanish projects MAT2013-41099-R and RyC-2010–06276. Use of the NSLS, Brookhaven National Laboratory was supported by the DOE BES (DE-AC02-98CH10886). H.A. and V.G. acknowledge support for them the Penn State NSF-MRSEC Center for Nanoscale Science grant (DMR-1420620). The authors would like to thank Dr. T. Sarkar in Uppsala University of original magnetism check.

Keywords: bulk oxides · cationic rearrangements · ferrimagnetic semiconductors · Mn_2FeMoO_6 · physical property tunneling

How to cite: *Angew. Chem. Int. Ed.* **2016**, *55*, 9862–9867
Angew. Chem. **2016**, *128*, 10016–10021

[1] J. H. Lee, et al., *Nature* **2010**, *466*, 954–958 (see the Supporting Information).
[2] J. B. Goodenough, *Chem. Mater.* **2014**, *26*, 820–829.
[3] E. Dagotto, *Science* **2005**, *309*, 257–262.
[4] V. Gopalan, D. B. Litvin, *Nat. Mater.* **2011**, *10*, 376–381.
[5] T. Varga, et al., *Phys. Rev. Lett.* **2009**, *103*, 047601 (see the Supporting Information).
[6] R. Aso, D. Kan, Y. Shimakawa, H. Kurata, *Sci. Rep.* **2013**, *3*, 2214.
[7] P. Kayser, M. J. Martínez-Lope, J. A. Alonso, M. Retuerto, M. Croft, A. Ignatov, M. T. Fernández-Díaz, *Inorg. Chem.* **2013**, *52*, 11013–11022.
[8] A. Aimi, T. Katsumata, D. Mori, D. Fu, M. Itoh, T. Kyomen, K. Hiraki, T. Takahashi, Y. Inaguma, *Inorg. Chem.* **2011**, *50*, 6392–6398.
[9] Y. Inaguma, A. Aimi, Y. Shirako, D. Sakurai, D. Mori, H. Kojitani, M. Akaogi, M. Nakayama, *J. Am. Chem. Soc.* **2014**, *136*, 2748–2756.
[10] A. J. Dos Santos-Garcia, E. Solana-Madruga, C. Ritter, D. Avila-Brande, O. Fabelo, R. Saez-Puche, *Dalton Trans.* **2015**, *44*, 10665–10672.
[11] A. A. Belik, Y. Matsushita, M. Tanaka, E. Takayama-Muromachi, *Angew. Chem. Int. Ed.* **2010**, *49*, 7723–7727; *Angew. Chem.* **2010**, *122*, 7889–7893.
[12] Z. J. Zhang, Z. L. Wang, B. C. Chakoumakos, J. S. Yin, *J. Am. Chem. Soc.* **1998**, *120*, 1800–1804.
[13] H. S. C. O'Neill, W. A. Dollase, *Phys. Chem. Miner.* **1994**, *20*, 541–555.
[14] S. Chen, Y. Wu, P. Cui, W. Chu, X. Chen, Z. Wu, *J. Phys. Chem. C* **2013**, *117*, 25019–25025.
[15] J. Reed, G. Ceder, *Chem. Rev.* **2004**, *104*, 4513–4534.
[16] J. Lee, A. Urban, X. Li, D. Su, G. Hautier, G. Ceder, *Science* **2014**, *343*, 519–522.
[17] R. Mathieu, S. A. Ivanov, I. V. Solovyev, G. V. Bazuev, P. Anil Kumar, P. Lazor, P. Nordblad, *Phys. Rev. B* **2013**, *87*, 014408.
[18] M.-R. Li, et al., *Angew. Chem. Int. Ed.* **2013**, *52*, 8406–8410; *Angew. Chem.* **2013**, *125*, 8564–8568 (see the Supporting Information).
[19] M.-R. Li, et al., *Adv. Mater.* **2015**, *27*, 2177–2181 (see the Supporting Information).
[20] M.-R. Li, P. W. Stephens, M. Retuerto, T. Sarkar, C. P. Grams, J. Hemberger, M. C. Croft, D. Walker, M. Greenblatt, *J. Am. Chem. Soc.* **2014**, *136*, 8508–8511.
[21] M.-R. Li, et al., *Angew. Chem. Int. Ed.* **2014**, *53*, 10774–10778; *Angew. Chem.* **2014**, *126*, 10950–10954 (see the Supporting Information).

[22] P. M. Woodward, A. W. Sleight, L.-S. Du, C. P. Grey, *J. Solid State Chem.* **1999**, *147*, 99 – 116.
[23] R. Shannon, *Acta Crystallogr. Sect. A* **1976**, *32*, 751 – 767.
[24] C. Lefevre, F. Roulland, A. Thomasson, C. Meny, F. Porcher, G. André, N. Viart, *J. Phys. Chem. C* **2013**, *117*, 14832 – 14839.
[25] M. Retuerto, J. A. Alonso, M. J. Martínez-Lope, J. L. Martínez, M. García-Hernández, *Appl. Phys. Lett.* **2004**, *85*, 266 – 268.
[26] N. F. Mott, *Conduction in non-crystalline materials*, 2nd. ed., Clarendon Press, Oxford, **1993**.
[27] J. I. Jang, S. Park, C. M. Harrison, D. J. Clark, C. D. Morris, I. Chung, M. G. Kanatzidis, *Opt. Lett.* **2013**, *38*, 1316 – 1318.
[28] B. A. Wechsler, C. T. Prewitt, *Am. Mineral.* **1984**, *69*, 10.
[29] A. Navrotsky, *Chem. Mater.* **1998**, *10*, 2787 – 2793.
[30] T. Yamanaka, Y. Komatsu, M. Sugahara, T. Nagai, *Am. Mineral.* **2005**, *90*, 1301 – 1307.

Received: December 7, 2015
Revised: February 7, 2016
Published online: May 20, 2016

